Kinetic Monte Carlo modeling of Y_2O_3 nano-cluster formation in radiation resistant matrices

G. Zvejnieks, A. Anspoks, E.A. Kotomin*, V.N. Kuzovkov

Institute of Solid State Physics, University of Latvia, Kengaraga Str. 8, LV-1063 Riga, Latvia

Abstract

As known, Y_2O_3 nano-clusters considerably increase radiation resistance of reactor construction materials. To model the nano-cluster formation kinetics, we propose the simplest possible mathematical model and perform kinetic Monte Carlo (KMC) simulations. We extended the KMC simulated results to the experimentally relevant times using autoregressive integrated moving average forecasting. Within the model, we have studied prototypical attractive interaction energies and particle concentrations, and compared the simulations with experiments. We have observed the standard Lifshitz-Slyozov-Wagner (LSW) theory, predicting the average cluster radius growth with time, $\overline{R} \sim t^{1/p}$, with p=3 in the long-time limit, for weak (0.1 eV) mutual particle attraction. However, the respective cluster growth rates in these KMC simulations are overestimated compared to the experiments. The best agreement with experiment is obtained for a medium (0.3 eV) and strong (0.5 eV) attractions, when nano-cluster formation occurs during *intermediate asymptotic* time scale, where power order p ranges from 5 to 7.6 depending on interaction, without reaching actually the LSW long-time limit. Such a stronger interaction leads also to a more compact {110}–faceted nano-clusters.

Keywords: Y_2O_3 nano-clusters, Oxide dispersion strengthened (ODS) steels, Coarsening, Ostwald ripening, Kinetic Monte Carlo

1. Introduction

New alloy materials with improved radiation damage resistance at elevated temperatures are required for future fission and fusion reactors [1]. In particular, Fe-Cr based ferritic steels with ultra high concentration of Y-O (or Y-Ti-O) nano-clusters are promising candidates for such materials [2]. However, it is a technological challenge to produce an alloy with a uniform distribution of nano-sized oxide clusters. One of the possibilities is to perform the mechanical alloying (of steel and yttria) with the following thermo-mechanical treatment [3, 4]. There are number of conditions in alloy processing that affect the final nano-cluster distribution, including: chemical composition of the alloyed materials (in particular, the amount of Ti adatoms [5, 6]), temperature and duration of the annealing stage [7–12].

In recent years there is a rising interest to establish experimentally the oxide nano-cluster growth kinetics. The average cluster radius time dependence in the form

$$\overline{R} \sim t^{1/p} \tag{1}$$

*Corresponding author
Email address: kotomin@latnet.lv (E.A. Kotomin)

with various power orders, p, (3 – LSW regime, 5 – pipe diffusion, or ≈6) was proposed to interpret the experiments [7–12]. To understand the underlying processes, oxide nano-cluster formation and growth experimental studies where accompanied by extensive theoretical studies using *ab initio*, first principle KMC methods as well as thermodynamic approach [13–16]. KMC simulations were used to study Y_2O_3 precipitation kinetics in α-iron as well as the effect of supersaturation [13]. The effect of vacancies on mobility of Y, Zr, Ti atoms was also studied from first principles [14]. The dislocation pipe diffusion (p=5) was proposed as a dominant mechanism in the semi-empirical thermodynamic and kinetic studies of oxide precipitation [15].

In this paper, using KMC simulations we study the precipitation process, starting from nano-cluster homogeneous nucleation till the cluster growth via Ostwald ripening (OR) mechanism, with a particular emphasis on the cluster growth kinetics. We use simplified Y_2O_3 formation model that allows us to make a direct quantitative comparison of an average cluster radii, cluster growth rate and cluster density with both available experimental and theoretical data. In the KMC simulations, we use *the standard model* and *the pair algorithm* approach [17] that was successfully applied earlier for studying complex kinetics both in 2D catalytic systems [18–20] and void self-organization in 3D [21]. In order to forecast cluster growth kinetic results beyond the scope of KMC calculation limits, we complement the KMC simulations with the autoregressive integrated moving average (ARIMA) method [22].

2. Physical basis of the model

Experimental observations demonstrate that on one hand, the cluster structures arising in the oxide dispersion strengthened (ODS) steels depend on the chemical composition of the material, i.e., the structures are determined microscopically by the particle types involved in the cluster formation and their interaction potentials. On the other hand, we are interested in the non-equilibrium structure formation kinetics in such a system of mobile and interacting particles. Formally, the kinetics of the microscopic model can be studied using KMC method. However, there are principal difficulties, since the underlying physical process of particle cluster formation is of the OR type. OR describes the time evolution of an inhomogeneous structure, where small cluster of particles dissolve and redeposit onto larger ones. In this study the characterization of OR process kinetics is of a particular interest, especially by approaching the long-time limit.

The studies of such asymptotics by KMC method is far from trivial. OR process is characterized by the time power law Eq. (1). Therefore, to obtain the non-redundant information, the time interval of data sampling should increase exponentially and simulation time should cover several orders of magnitude. With such a sampling, the number of large clusters, that are the primary objects of interest, is decreasing approximately exponentially in the long-time limit thus worsening the statistics. For example, in order to extend the simulation for a few (exponential) steps with identical statistics, one needs to increase twice the lattice size. As the result, the computer time required for simulations increases eightfold. One can propose naively to extrapolate to the long-time limit of KMC simulations using LSW theory [23, 24]. This approach, however, has some shortcomings. On one hand, the LSW theory operates with two competitive concepts of diffusion and reaction. Particle interactions are incorporated in the theory indirectly by using macroscopic surface tension and reaction rate. (In general a surface tension might depend on the size of the clusters and position of parameters in the phase diagram [25]).

Then, the theory predicts different OR behavior, see Eq. (1), in the long-time limit for either diffusion (p=3) or reaction (p= 2) limited cases, respectively. It is predicted that the proportionality coefficients depend on solubility concentration and thus the rates are independent of total particle concentration in the system.

On the other hand, the KMC simulations are based on the microscopic model with a given particle interaction, concentration and temperature. The surface tension originates from attractive particle interactions, that lead to formation of clusters, and is not introduced directly in the model. Moreover, no assumption is made regarding the slowest process and the particle concentration effects can be studied directly. The topmost advantage is that KMC allows us to explore the whole process of particle cluster formation, starting from nucleation till OR regime, and determine the intermediate asymptotic kinetics that arise before the LSW long-time limit. In such the case, the asymptotics corresponds to the auto-model solution between two limiting parameter values (two times t_{min} and t_{max}). In other words, for observation times, t, (t_{min}<t<t_{max}) the characteristic distributions are obtained using similarity transform. Correspondingly, the kinetics of the process is characterized by fundamental time power laws [26, 27].

Importance of the intermediate asymptotic is due to the following specific features of the ODS steel experiments: a few nanometer large clusters typically grow during a few hours (or a few hundred of hours in dedicated kinetics studies) according to Eq. (1) with a power orders p=5 or 6.28 interpreted as the pipe diffusion [11] . However, as shown in this paper, similar power orders could arise also as an intermediate asymptotic before reaching the LSW regime. These results hold for a simple 3D model with particle diffusion and interaction, without any other (e.g., pipe) diffusion mechanism.

In the KMC simulations of intermediate asymptotics, development of the detailed microscopic model could cause substantial difficulties. Such a model requires knowledge of all the elementary microscopic processes including all types of relevant particles, their interactions and mobility parameters and is indeed actively developed during last years, see [13–16]. On one hand, such an approach with interaction estimates from the first-principle calculations [28, 29], when used in KMC simulations [20], might lead within the uncertainty of parameters to a wide variety of system behaviors. On the other, precise interaction energies between particles determine mainly the short-range order of particles within the clusters rather than the asymptotic time dependence of average cluster radius. Therefore, in this paper, we simplify the process of detailed Y_2O_3 cluster formation in ODS steels to study the fundamental cluster growth laws.

3. Model

The detailed models that take into account different types of particles (Y, Ti, O and Fe vacancies), their microscopic interactions and diffusion where used in previous KMC simulations [13, 30–32]. However, in this paper, since the focus is on the intermediate- and long-time kinetics of the cluster growth, we propose the simplified Y_2O_3 nano-cluster formation model in α-iron based on the following assumptions. (i) Since the kinetics is governed mainly by the particle transport, we consider the yttria nano-clusters as objects without the inner structure. We assume that clusters are formed by the effective particles, A, (that represent Y, O atoms and Fe vacancies) with concentration, c_A, and can be characterized by an effective nearest neighbor (NN) attractive interaction, ε. The latter is our only fit parameter in the model and describes the average interactions between A particles.

D_0 [m^2/s]	E_{act} [eV]	ν_0 [s^{-1}][d]	$\nu(1100°C)$ [s^{-1}]
10^{-5}	3.10[a]	10^{15}	4×10^{3}
8.0×10^{-7}	2.26[b]	10^{14}	5×10^{5}
2.4×10^{-6}	2.14[c]	3×10^{14}	4×10^{6}

Table 1: Experimental[a] [13, 37] and theoretical [b][14], [c][36] mobility parameters for Y particles in α-iron. [d]Estimates of attempt frequencies are obtained from Eq. (3).

Let us estimate the concentration of particles A that correspond to a typical Y_2O_3 concentration of 0.3 wt % in ODS steels. The Y_2O_3 unit concentration per site (occupancy) could be found from

$$c_{Y_2O_3} = \frac{0.3wt\%/A_{Y_2O_3}}{0.3wt\%/A_{Y_2O_3} + 99.7wt\%/A_{Fe}}\,, \tag{2}$$

where $A_{Y_2O_3} = 226$ u and $A_{Fe} = 56$ u are atomic weights of Y_2O_3 and Fe, respectively. We assume that Y_2O_3 forms a coherent [16] bixbyite structure [33] (lattice constant 1.06 nm [34]) within the α-iron lattice (lattice constant a_0=0.286 nm [35]). For a bixbyite structure additional Fe vacancies are required to be built-into nano-cluster leading to a $Y_2O_3\mathrm{Vac}_3^{Fe}$ complex unit that occupies 8 Fe body-centered cubic (bcc) lattice sites. Then A particles (site) concentration is found from $c_A = 8\,c_{Y_2O_3}$ that for Y_2O_3 concentration of 0.3 wt % corresponds to $c_A = 0.006$.

Extension of the model, by addition of different particle sorts, have negligible effect on concentration. For example, when 0.1Ti is added to the system, the A particle concentration increases till $c_A \sim 0.007$, if Ti doesn't build into Y_2O_3 cluster structure and each Ti atom within the cluster requires additional bcc Fe site. Contrary, if Ti builds into the existing Y_2O_3 bixbyite structure cluster by occupying existing there Fe vacancies, the A particle concentration remains unchanged. For a completeness of definition, let us introduce a monomer concentration, c_0', by excluding the volume occupied by all clusters.

(ii) The mobility of A particles should correspond to the slowest moving particles that form Y_2O_3 bixbyite structure. Since the clusters grow in a layer by layer mode, the slowest moving particle will provide the rate limiting step. In a general form A particle jumps to the NN empty lattice site are characterized by the diffusion coefficient

$$D = D_0 \exp[-E_{act}/(k_BT)] = l^2\nu/z = l^2\nu_0/z \exp[-E_{act}/(k_BT)]\,, \tag{3}$$

where l is jump length, z number of NN and ν_0 attempt frequency. In the bcc lattice with eight nearest neighboring sites ($z = 8$) the jump length is $l = \sqrt{3}a_0/2$.

It is known that experimentally determined Y particle diffusion, Table 1, is the slowest while mobilities of Fe vacancies, Ti and O are much higher. However, experimental and theoretical Y particle diffusion coefficient estimates (and hopping rates), Table 1, differ by several orders of magnitude at the experimentally relevant temperature 1100°C. It is proposed in Ref. [36] that Y diffusion in experiments could be altered by oxygen and Fe vacancies, which strongly bound Y atom. Since we are interested in the effective Y diffusion estimate, where complex microscopic jump details are already taken into account (similarly to the effective A particle that accounts for Y, O, Fe vacancies) further we use the experimental Y hopping rate estimates by Alinger and Hin [13, 37].

In computer simulations, we consider bcc lattice of size $L\times L\times L = V$ (where L is lattice side length which varies from $L = 80$ till $240a_0$) with $N = 2V/a_0^3$ sites and

periodic boundary conditions. Particles A are distributed randomly within the lattice at the beginning of simulations. Particles are mobile and can hop to the nearest free site. This step is implemented in KMC simulations using *the pair algorithm* and *the standard model dynamics* [17]. The pair algorithm contains the following steps:

- A NN pair is randomly selected from all possible pairs in the bcc lattice.
- If the pair contains a single vacancy, O, and particle, A, (OA or AO), the hoping step (exchange of positions AO or OA, respectively) is performed, if a random number (RN) normalized to unity is less that step rate, $\nu_{\alpha\beta}$,

$$\nu_{\alpha\beta} = \frac{2\nu}{1 + \exp\left(-(n_\alpha - n_\beta)\varepsilon/(k_B T)\right)}, \tag{4}$$

  where α and β are the first and second site of the pair. The jump rate of a single free particle, ν, from Eq. (3) is modified, $\nu_{\alpha\beta}$, in Eq. (4) to take into account the interaction between particles. The standard model dynamics [17] allows us to introduce the step rate symmetrically (irrespective of the direction of the jump, e.g, $OA \rightleftharpoons AO$) unlike to, e.g., the Metropolis dynamics [38]. The negative interaction energy used for a pair of particles in NN positions, ε, corresponds to their mutual attraction; n_α and n_β are the numbers of occupied NN positions in the initial and final configurations, respectively. Here it is convinient to introduce a dimensionless interaction energy $\epsilon = \varepsilon/(k_B T)$.

- Time is updated by a fixed increment

$$\Delta t = \frac{1}{N\nu} \tag{5}$$

  and the algorithm returns to the first step, until the final simulation time is reached. In the KMC simulations, we use dimensionless time $\tau = t\nu$ and return to dimensional time, t, only when we make a comparison with experimental results.

The long-time behavior (LSW-type power laws) are examined in KMC at the temperature 1100 °C for three particle concentrations, c_A, (0.005, 0.1, and 0.2), and three prototypical interaction energies, ε: weak (-0.1), medium (-0.3), and strong (-0.5 eV) that correspond to the dimensionless interactions $\epsilon = -0.85$, -2.54, and -4.23, respectively. In order to increase the accuracy of KMC simulations, we repeat and average results of 10 calculations, unless specified otherwise.

4. KMC simulation analysis

4.1. Phase diagram

In order to analyze the spatial particle structures, we define a particle cluster as a connected (in nearest neighbor (NN) sense) group of A particles in the bcc lattice. Cluster formation strongly depends on both, A particle concentration, c_A, and dimensionless interaction energy, ϵ, as shown in the solubility-supersolubility diagram, Fig. 1. Similarly to Ref. [39], we find here three zones: (i) the stable (unsaturated) zone where spontaneous nucleation and cluster growth is impossible; (ii) The metastable (supersaturated) zone, where spontaneous nucleation is improbable, but a cluster seed placed in the metastable zone would experience growth; (iii) The unstable (supersaturated) zone, where spontaneous nucleation is probable, but not inevitable.

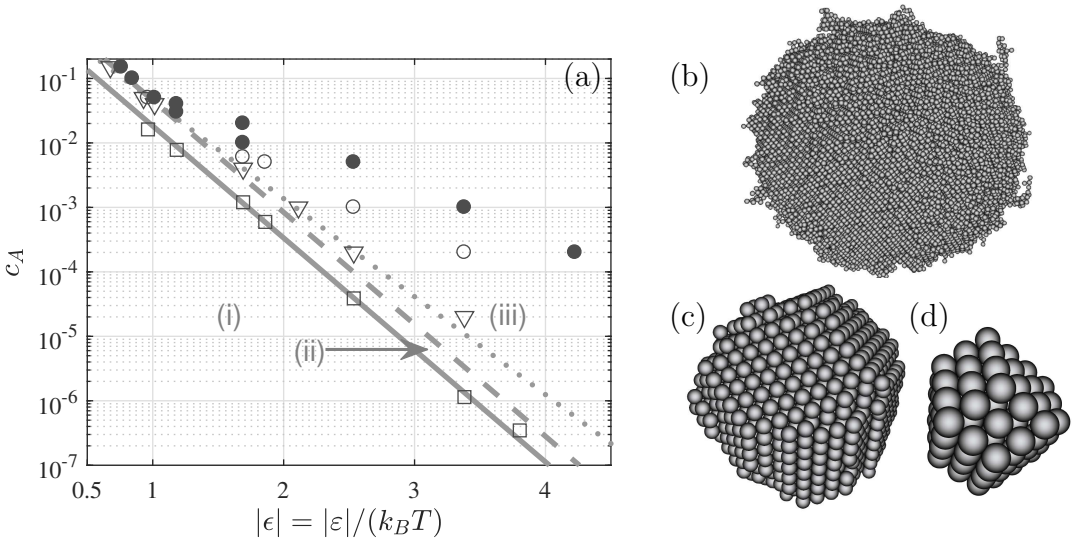

Figure 1: Solubility–supersolubility phase diagram (a). Three zones could be distinguished: (i) the stable, (ii) the metastable and (iii) the unstable. KMC simulations demonstrate particle aggregation (full circles), single large cluster growth (open circles), and no cluster growth regimes (down triangles), respectively. Solubility estimates from KMC, c_∞^{GT}, are given by squares. A solubility, $c_\infty^A(\epsilon)$, and two supersolubility, $c_{nuc}(\epsilon)$, fit to the Arrhenius equations are shown by solid and dashed/dotted lines, respectively. Snapshots of average cluster size, r_n, Eq. (8), for (b) weak ($\epsilon = -0.85$) $r_{105866} = 6.7$ nm, (c) medium ($\epsilon = -2.54$) $r_{1801} = 1.7$ nm and (d) strong ($\epsilon = -4.23$) $r_{123} = 0.7$ nm interactions at time $\tau = 3.3{\times}10^6$ and particle concentration c_A=0.1. Each data point is obtained from a single KMC calculation.

The solubility concentration, $c_\infty(\epsilon)$, that separate the stable-(i) and the metastable-(ii) zone can be found from KMC simulations that lead to an equilibrium configuration with a single spherical cluster with a radius, r, surrounded by single particles (flow of particles to and from the cluster are equal). KMC simulations that give such a configuration, might bypass the OR stage when just a single nucleus (and thus a single cluster) is created in the lattice often after a prolonged incubation period, see empty circles in Fig. 1. The solubility concentration, $c_\infty^{GT}(\epsilon)$, can be estimated using the equilibrium monomer concentration, $c_0'(\tau \to \infty)$, at a single spherical cluster by excluding the volume of the cluster and the well-known Gibbs-Thomson relation [40]

$$c_0'(\tau \to \infty) = c_\infty^{GT}(\epsilon) \exp\left(\frac{l_c}{r}\right), \text{ where} \tag{6a}$$

$$l_c = \frac{2\gamma v_1}{k_B T}, \tag{6b}$$

$$\gamma = \frac{(z_s - z_b)\varepsilon}{2s_1}, \tag{6c}$$

$$c_\infty^A(\epsilon) = c_\infty^0 \exp(-k_\infty|\epsilon|), \tag{6d}$$

where l_c is the capillarity length and v_1 volume of a single particle. The specific interfacial energy, γ, using a simplified bond-counting model could be estimated from Eq. (6c), where s_1 is a single-particle exposed surface area, z_s and z_b are numbers of occupied bonds for a particle at the surface and in the bulk of the cluster, respectively. For compact clusters formed by {110}–facets (Fig. 1c,d) the number of bonds can be estimated as $z_s = 6$ and $z_b = 8$, respectively, that, in turn, leads to a surface area, $s_1 = \pi r_1^2$. The solubility $c_\infty^{GT}(\epsilon)$ estimates obtained using Eqs. (6a–6c) are shown by square symbols in Fig. 1. On the

other hand, the solubility concentration, $c_\infty(\epsilon)$, can be estimated in the Arrhenius form Eq. (6d) [41], where $c^0_\infty = 1.0$ and $k_\infty = 4.0$, see solid line in Fig. 1. (The c^0_∞ coincides with the bulk concentration in the $T \to \infty$ limit, while $k_\infty = 4.0$ corresponds to half of the bcc lattice coordination number [41].) Both estimates agrees well, $c_\infty(\epsilon) \equiv c^{GT}_\infty(\epsilon) = c^A_\infty(\epsilon)$, indicating that Eqs. (6) are self-consistent, except for weak interactions, $|\epsilon| < 1$. In the latter case the particle cluster is loose, see Fig. 1b, and the simple interfacial energy estimates Eq. (6c) are no longer applicable, since for diffuse clusters there exist no simple estimate of the occupied surface bound number, z_s, and exposed particle surface, s_1.

Determination of metastable-(ii) and the unstable-(iii) zone separation (the supersolubility curve) is more challenging, since its position, among other things, is affected by the history of the sample [39]. In KMC simulations we find that weak attraction and small concentration strongly suppress cluster nucleation and thus hinder the reaching of the critical cluster size, see down-triangles in Fig. 1. Moreover, there is a region in the unstable zone where just a single particle cluster is formed in the lattice after a certain incubation time, see open circles in Fig. 1. The incubation time increases either by approaching the supersolubility curve in the phase diagram and/or by decreasing the lattice size. The supersolubility curve, $c_{nuc}(\epsilon)$, can be estimated in the Arrhenius form

$$c_{nuc}(\epsilon) = c^0_{nuc} \exp(-k_{nuc}|\epsilon|)\,, \tag{7}$$

however, with some uncertainty. Here we define that there is no spontaneous nucleation in a KMC simulation run, when for a 3D lattice of size, $L = 120a_0$, no stable clusters are formed during $\tau = 4{\times}10^6$ (16 min at 1100 °C). It should be noted, that larger lattice sizes or longer waiting times can still initiate nucleation. Then for the supersolubility approximation Eq. (7) the two fits are possible: (i) a more conservative approach – when $c_{nuc}(\epsilon)$ is proportional to $c_\infty(\epsilon)$ with $c^0_{nuc} = 2.5$ and $k_{nuc} = 4.0$ (dashed line in Fig. 1), or (ii) less conservative approach, that is based on our definition of absent-nucleation in KMC simulations, that leads to the parameters $c^0_{nuc} = 1.5$ and $k_{nuc} = 3.5$ (dotted line in Fig. 1).

Particle nucleation and growth takes place in the KMC simulations when the starting random distribution of A particles exceeds the supersolubility curve, $c_A \approx c'_0(\tau = 0) > c_{nuc}(\epsilon)$, for a given interaction energy, ε, and temperature, T, see phase diagram (full circles) in Fig. 1. It should be noted that the largest concentration that could be randomly distributed in the bcc lattice without formation of percolating cluster, $c_A \lesssim 0.18$ (the bond percolation threshold [42]). For subpercolation concentrations two scenarios are possible with the advance of time – nucleation still continues if the remaining monomer concentration (taking into account the cluster excluded volume) is sufficient, $c'_0(\tau) > c_{nuc}(\epsilon)$. However, if the monomer concentration decreases below the supersolubility limit, $c'_0(\tau) < c_{nuc}(\epsilon)$, the nucleation is suppressed. In the latter regime, the existing clusters could grow on the expense of either other clusters (OR) or, in a case of a single cluster, on other monomers if $c'_0(\tau) > c'_0(\tau \to \infty)$.

4.2. Particle distribution function

Let us now quantitatively analyze the cluster growth in the unstable-(iii) zone. By performing the cluster analysis we find sizes, n, of each cluster in the lattice at time, τ. Due to two atoms in the bcc unit cell, we can estimate the cluster volume as $v_n = n\,a_0^3/2$. Then assuming that a cluster of n particles has a spherical shape, the corresponding

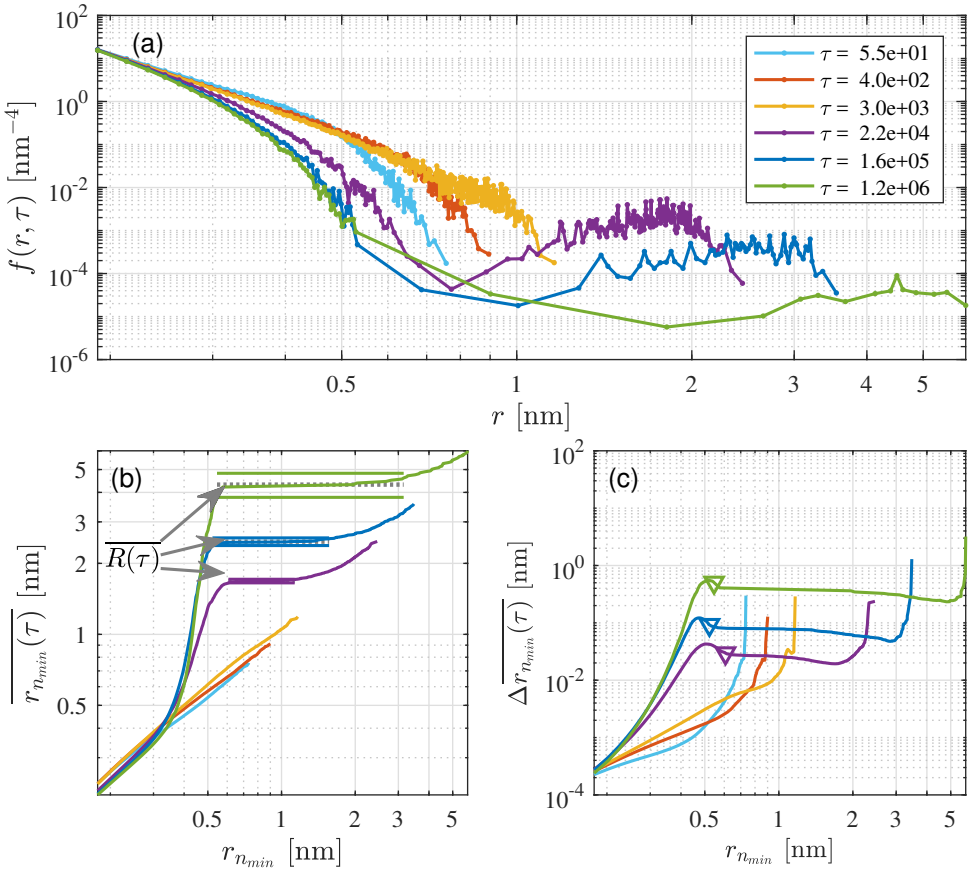

Figure 2: Cluster density analysis in the limit of weak attraction, $\epsilon = -0.85$: (a) PDF, (b) average cluster radius dependence on n_{min} (n_{min} independent average cluster radius, $\overline{R(\tau)}$, marked as dotted gray lines), and (c) accuracy of average cluster radius estimates. $\overline{R(\tau)}$ accuracy estimate marked by down triangles in (c) and plotted as a horyzontal lines in (b). Data are obtained from a single KMC simulation with parameters: $L = 240a_0$, $c_A = 0.1$, $\varepsilon = -0.1$ eV, $T = 1100$ °C.

cluster radius could be found as

$$r_n = \left(\frac{3n}{8\pi}\right)^{1/3} a_0\,. \tag{8}$$

The number of clusters is examined using the particle distribution function, $f(r,\tau)$, (PDF) [24]. The PDF is a discrete function due to an integer number of particles in a cluster, n, see Eq. (8):

$$f(r,\tau) = \{f(r_1,\tau), f(r_2,\tau), \ldots, f(r_{n_{max}},\tau)\}\,, \text{ where} \tag{9a}$$

$$f(r_n,\tau) = \frac{1}{V}\lim_{\Delta r_n \to 0} \frac{M\left(r_n, r_n+\Delta r_n, \tau\right)}{\Delta r_n}\,, \tag{9b}$$

and $M\left(r_n, r_n+\Delta r_n, \tau\right)$ is the number of clusters in volume, V, having radii, r, between r_n and $r_n + \Delta r_n$ at time τ. For the PDF calculation the bin sizes Δr_n in Eq. (9b) on the one hand should be as small as possible, while on the other hand they should contain a sufficiently large number of clusters, to reduce the statistical error. In our PDF estimate, each individual bin size is increased adaptively, till it contains at least two clusters, $M \geq 2$, that ensures the PDF continuity and smoothness, Fig. 2a, especially for large radius values.

The average cluster size can be defined as the first momentum, using Eqs. (8,9b)

$$\overline{r_{n_{min}}(\tau)} = \frac{\int r f(r,\tau) dr}{\int f(r,\tau) dr} = \left(\frac{3}{8\pi}\right)^{1/3} a_0 \frac{\sum_{n=n_{min}}^{n_{max}} n^{1/3} M(r_n,\tau)}{\sum_{n=n_{min}}^{n_{max}} M(r_n,\tau)}, \tag{10}$$

where the last term here is independent on the bin size Δr. Radius at n_{max} should account for the largest cluster in the lattice, but selection of n_{min} is a non-trivial task [25] and will be discussed below. The classical rate theories that estimate time dependence of average cluster radius neglect the cluster nucleation and coalescence [43]. However, nucleation is intrinsic process in KMC simulations that is observed in PDF as a number of small-radii clusters, see, Fig. 2a, when scaled monomer concentration, c_0', exceeds the supersolubility concentration, $c_{nuc}(\epsilon)$, in Fig. 1. The shape of PDF remains qualitatively similar until $\tau = 3{\times}10^3$without the characteristic cluster size present in the system. However, after this incubation time, the shape of PDF qualitatively changes, from $\tau = 2.2{\times}10^4$ in Fig. 2a, when the group of large clusters emerges and is observed as a second maximum in the PDF. These clusters grow further according to the OR rules and will be in the focus of our further analysis. The contribution of small clusters in the PDF thus should be ignored. We achieve this goal by neglecting the cluster sizes smaller that n_{min}.

In order to set the n_{min}, let us first determine the $\overline{r_{n_{min}}(\tau)}$ dependence on $r_{n_{min}}$. The average cluster radius increases as clusters with sizes smaller than n_{min} are excluded from averaging in Eq. (10), Fig. 2b. Finally, the plateau regions (if present) in $\overline{r_{n_{min}}(\tau)}$ figure correlate with the minima of PDF function, Fig. 2a, and can be used as the n_{min} independent average cluster radius estimates by excluding the nucleation contribution

$$\overline{R(\tau)} = \lim_{n_{min}} \overline{r_{n_{min}}(\tau)} \approx const\,. \tag{11}$$

When no such plateau region exists, e.g., during the incubation time, we assume that no characteristic cluster size exists in the system. The accuracy of the average cluster radius for each $r_{n_{min}}$ can be estimated using the standard deviation, S, and Student's two-sided t-distribution [44],

$$S = \sqrt{\frac{1}{n_{max}-n_{min}} \sum_{n=n_{min}}^{n_{max}} (r_n(\tau) - \overline{r_{n_{min}}(\tau)})^2}, \tag{12a}$$

$$\Delta\overline{r_{n_{min}}(\tau)} = \frac{S}{\sqrt{n_{max}-n_{min}+1}} t_{1-\alpha/2, n_{max}-n_{min}} \tag{12b}$$

with significance level $\alpha = 0.05$ and $n_{max} - n_{min}$ degrees of freedom, Fig. 2c. From here the accuracy of the n_{min} independent average cluster radius, $\overline{R(\tau)}$, can be estimated using the corresponding $r_{n_{min}}$ (down-triangles and horizontal lines in Fig. 2c-b, respectively).

The shape of PDF function changes qualitatively for a medium, $\epsilon = -2.54$, and strong, $\epsilon = -4.23$, interactions, Fig. 3, comparing to the weak one. Namely, with an increase of time, the number of small clusters decreases in PDF, indicating that particles for the medium and strong interactions tend to be bound to clusters rather than remain as monomers. The peculiar PDF behavior is observed in the limit of a strong attraction and times larger than $\tau = 1.6{\times}10^5$. Despite the repeating calculations, ten times with

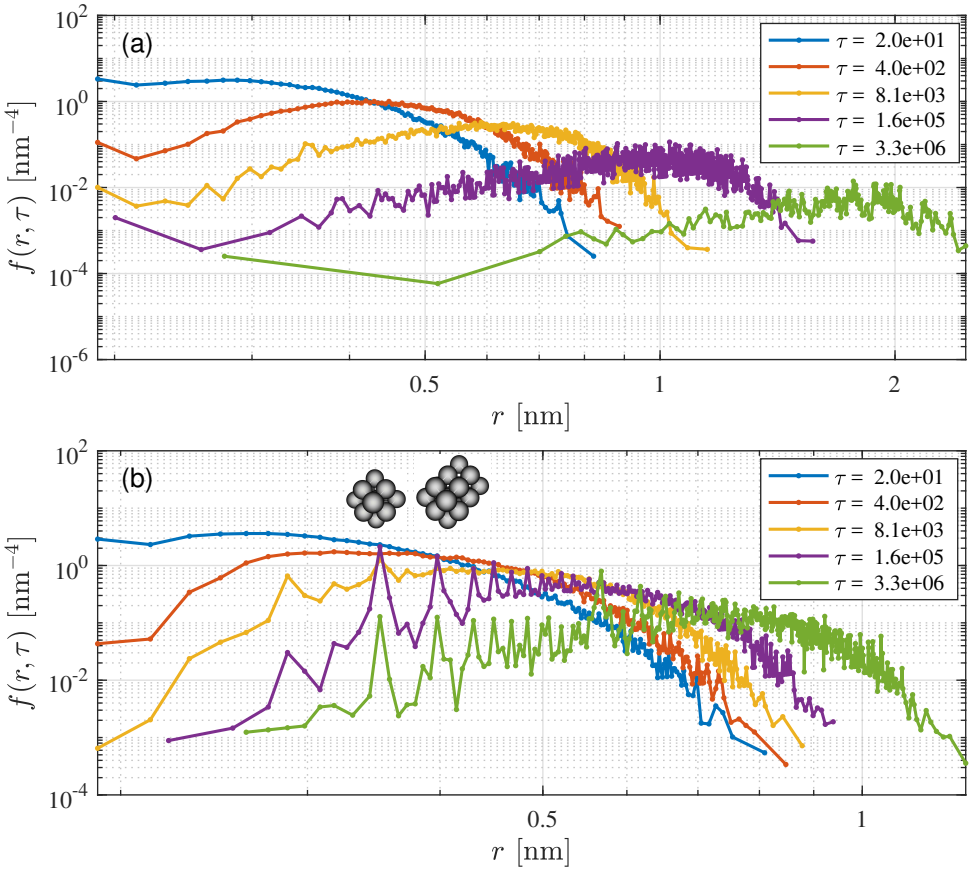

Figure 3: PDF for attractive: (a) medium, $\epsilon = -2.54$, and (b) strong, $\epsilon = -4.23$, interactions. Long living stable clusters of magic numbers $n = 15$ and 22 corresponding to the maxima of PDF functions at $r_{15} = 0.35$ and $r_{22} = 0.39$ nm at $\tau = 1.6{\times}10^5$ and $3.3{\times}10^6$, respectively are shown in insets of (b). Data are obtained as average over 10 independent KMC simulation with parameters: $L = 80a_0$, $c_A = 0.1$, $\varepsilon = -0.3$ (a) and -0.5 eV (b), $T = 1100$ °C.

the following averaging, the PDF function contains several long-living maxima for certain r values, e.g., $r_{15} = 0.35$ and $r_{22} = 0.39$ nm, Fig. 3b. These radii correspond to the most stable {110}–faceted clusters consisting of magic particle numbers $n = 15$ and $n = 22$, respectively. Due to surface particles that has six NN particle pairs (and edges with four NN pairs) they require more time to be disassembled, see insets in Fig. 3b.

4.3. Power laws

Let us now analyse quantitatively the cluster growth kinetic. Earlier different kinetic laws, Eq. (1), have been proposed for different limiting cases: viscous flow ($p = 1$), interfacial control ($p = 2$), volume diffusion ($p = 3$), interfacial diffusion ($p = 4$), and pipe diffusion ($p = 5$) [45], respectively. Our KMC simulations correspond to the volume (3D, $p = 3$) diffusion case and thus the long-time behavior of the OR process is predicted by three power laws of the LSW theory

$$\overline{R(\tau)} \propto k_1\tau^{1/3} = k_1' t^{1/3}\,, \tag{13a}$$

$$c_0'(\tau) - c_\infty(\epsilon) \propto k_2\tau^{-1/3} = k_2' t^{-1/3}\,, \tag{13b}$$

$$\rho_{cl}(\tau) \propto k_3\tau^{-1} = k_3' t^{-1}\,, \tag{13c}$$

for average cluster radius, degree of supersaturation and cluster density [23, 40, 43], respectively. Equations (13) are valid for $\overline{R(\tau)} \gg R_{c0}$, where the initial critical radius

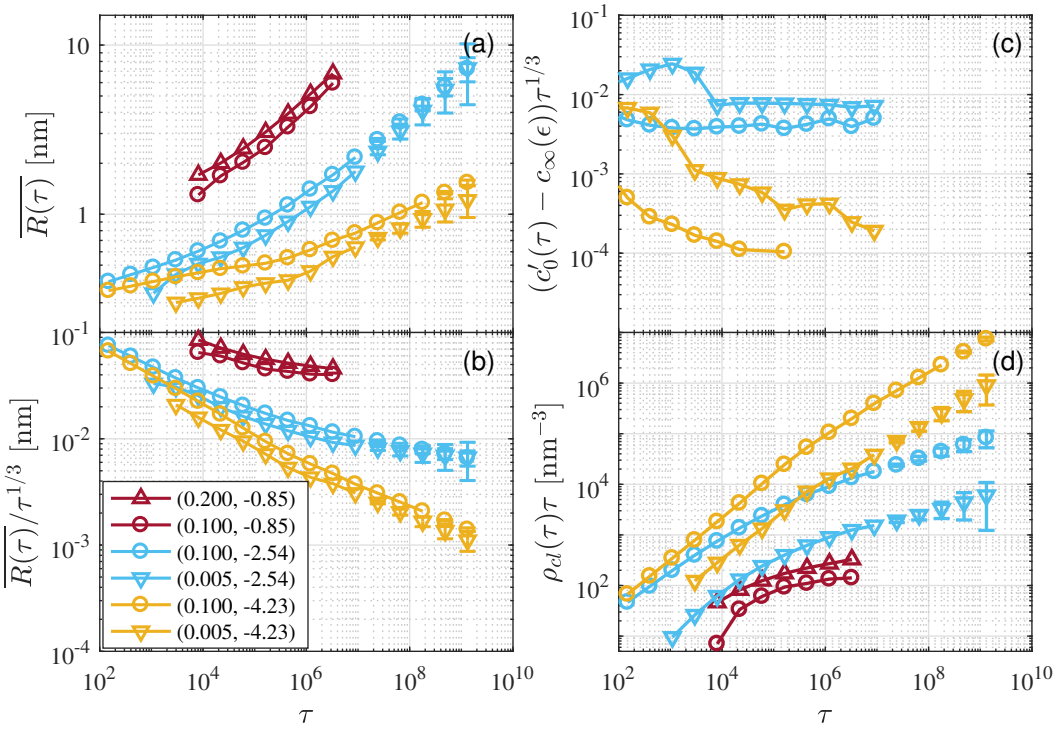

Figure 4: Average cluster radius (a) and LSW power law (b-d) asymptotic behavior. KMC simulations and the corresponding ARIMA(0,2,0) model forecasts are given with and without the solid lines, respectively. Particle concentration and dimensionless interactions are given as pairs (c_A, $\epsilon = \varepsilon/(k_BT)$). All data are obtained as average over 10 independent KMC simulations except (0.1,-0.85) case where a single calculation is performed. We use $L = 80a_0$ for (0.1,-4.23) and (0.1,-2.54); $L = 140a_0$ for (0.005,-4.23) and (0.005,-2.54); $L = 180a_0$ for (0.2,-0.85) and $L = 240a_0$ for (0.1,-0.85).

for coalescence corresponding to the starting supersaturation is $R_{c0} = l_c c_\infty(\epsilon)/(c_0'(0) - c_\infty(\epsilon))$ [23]. This condition is fulfiled in our simulations and we neglect the R_{c0} contribution in Eq. (13).

The increase of average cluster radius, $\overline{R(\tau)}$, with time in KMC simulations demonstrates strong dependence on particle interaction energy, ϵ, Fig. 4a. The accuracy of the KMC estimates are of the order of figure symbols and therefore not shown on the plots. A weak attraction leads to a faster growth of clusters than a strong one, due to shorter time needed for particles to detach from existing clusters, leading to a faster disappearance of small clusters and growth of the large ones. Contrary, a strong attraction increases time needed for particle detachment and thus slows down the large cluster growth at the expense of the small ones.

The KMC simulations show that cluster growth kinetics approaches the LSW long-time limit faster ($\tau > 10^6$) for weak interaction, while for medium and strong interactions the long-time limit lies beyond our simulation times and could be estimated only from below using forecasting results $\tau > 10^8$ and $> 10^9$, respectively, Fig. 4b–d. By comparing the average cluster radius, rate of cluster growth and cluster concentration, Fig. 4a,b,d, one can conclude that the weak interaction leads to a small number of fast growing large clusters (Fig. 1b), while medium and strong interactions produce larger number of slower growing smaller clusters (Fig. 1c,d).

Particle concentration, c_A, plays a principal role in kinetics along with dimensionless interaction, ϵ, that determines the conditions for a cluster formation. Thus, for a weak attraction and small concentration, $c_A = 0.005$, the cluster formation is absent, Fig. 1.

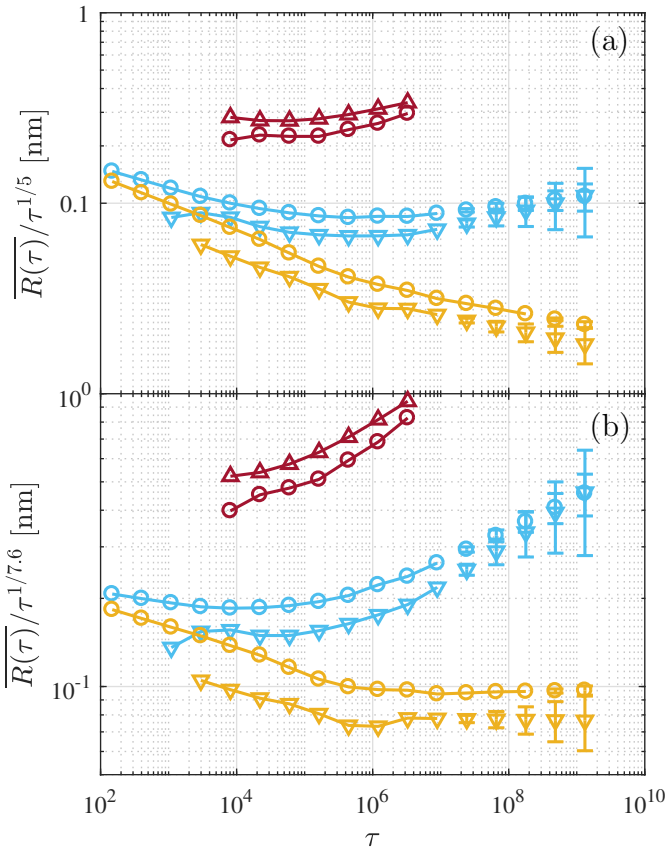

Figure 5: Average cluster radius scaling with different dimensionless time powers, Eq. (1), demonstrating intermediate asymptotic regime (horizontal plateau region) for: (a) p=5 (medium interaction) and (b) p=7.6 (strong interaction), respectively. The abbreviations are identical to Fig. 4.

When cluster formation is possible, the particle concentration most strongly affects the cluster density in simulations, $c_A \propto \rho_{cl}$, Fig. 4d, while the average cluster radius and the radius growth rate are only slightly affected, Fig. 4a,b. The degree of supersaturation, Fig. 4c, for medium and strong interactions demonstrate the tendency towards saturation. It also implies that in the long-time limit the disparities arising for different concentrations disappear and monomer concentration (taking into account the cluster excluded volume), c_0', tends to the solubility concentration, $c_\infty(\epsilon)$, according to the LSW theory predictions. Unfortunately, the degree of supersaturation for a weak attraction remains undetermined (leading to unphysical result $c_0' < c_\infty(\epsilon)$) due to simplified bond counting model used in the interfacial energy, γ, estimate Eq. (6c), that is not applicable for loose clusters, Fig 1b.

Since the KMC simulations are limited by our computing capabilities, we performed the power law forecasting until times $\tau = 10^9$, see symbols without line in Fig. 4a,b,d. The autoregressive moving average model has been applied earlier for analysis and simulation of time series containing noise, that arise, e.g., in tokamak experiments [46, 47]. In this paper, we use autoregressive integrated moving average ARIMA(p,d,q) model [22] that is well suited for nonstationary series. We found that the ARIMA(0,2,0) is the simplest parameter-free model that describe the KMC data,

$$y_\theta = 2y_{\theta-1} - y_{\theta-2} + \zeta_\theta, \tag{14}$$

where y and θ are the corresponding KMC simulation data in the logarithmic form and logarithmic time step index, respectively, and ζ_θ is the noise term at step θ. The

forecasting, $\hat{y}_{\theta+h}$, for h steps ahead can be done using Eq. (14), see Fig. 4, with the following accuracy estimate [22]

$$\Delta\hat{y}_{\theta+h} = u_{\alpha/2}\left(1+\sum_{k=1}^{h-1}k^2\right)^{1/2} s_\zeta, \tag{15}$$

where s_ζ is the standard deviation of the white noise process ζ_θ and $u_{\alpha/2}$ is the deviate exceeded by a proportion $\alpha/2$ of the unit normal distribution.

Finally, we note that determination of the kinetics order p from the experimental data may be hindered by the transition (intermediate) type kinetics. This is especially critical if the effective particle interaction, ϵ, is medium or strong and the intermediate kinetics may be observed at least until times $\tau = 10^8$ and $\tau = 10^9$, see Fig. 4, respectively. When such data are scaled to different p orders, they could demonstrate plateau-like behavior. However, as demonstrated in our KMC simulations with medium interaction and scaling with power $p = 5$, Fig. 5a, the conclusion regarding the pipe type diffusion in this case is misguided, since instead we are observing the intermediate asymptotic kinetic.

Similarly, for a strong interaction the horizontal plateau region (for the intermediate kinetics) is obtained in KMC simulations with $p = 7.6$, Fig. 5b. Thus, the average cluster radius growth during intermediate asymptotic stage could be described by, Eq. (1), with different orders p depending particle interaction, ϵ, and a stronger interaction leads to both larger exponent p and longer intermediate stage region.

5. A comparison of computer simulation results with LSW theory and experiments

The characteristic data of a cluster formation and growth (average cluster radius, $\overline{R(\tau)}$, cluster density, ρ_{cl}, and cluster growth rate, k_1') from the KMC simulation at experimentally relevant time and temperature limits from Fig. 4 are collected in Table 2. We find that KMC simulations can be performed till $\tau \sim 10^7$. ARIMA forecasting allows one to extend times by several orders, e.g., till $\tau \sim 10^9$, however, the accuracy of the estimates are quickly reducing, Eq. (15). By using the experimental Y particle jump rate at temperature 1100 °C, see Table 1, we find that KMC and ARIMA forecasts correspond to the physical time estimates of 40 min and 90 h, respectively, Table 2.

In the KMC we have simulated concentration range from $c_A = 0.005$ up to 0.2 (fortyfold increase) and found, that such system characteristics as cluster radius and growth rate are independent on concentration, see e.g., Table 2. We observe that only the cluster density is highly sensitive to concentration and for twentyfold concentration increase the cluster density increases by one order. Therefore the KMC concentration, $c_A = 0.005$, can be well used as an A particle concentration estimate in the considered experiments, Table 2.

The characteristic data can also be evaluated from the LSW theory, Eq. (13), by using coefficients [23]

$$(k_1')^3 = k_1^3\nu = \frac{4}{9}Dl_c c_\infty(\epsilon)\,, \tag{16a}$$

$$(k_2')^{3/2} = k_2^{3/2}\nu^{-1/2} = \frac{3l_c c_\infty(\epsilon)}{2\sqrt{D}}\,, \tag{16b}$$

$$k_3' = k_3\nu^{-1} = (2Dl_c c_\infty(\epsilon))^{-1}\,. \tag{16c}$$

The average cluster radius, $\overline{R(\tau)}$, and growth rate, k_1', predicted by the LSW theory agree well with the KMC data for a weak attraction ($\epsilon = -0.85$) (except the cluster density that is overestimated by two orders of magnitude), since KMC simulations at times $\tau = 10^6$ have reached a long-time limit without prolonged intermediate asymptotic regime, Table 2. Contrary, for medium and strong interactions the LSW regime is still unreached until $\tau < 10^8$ and $\tau < 10^9$, respectively, see Fig. 4a,b,d. As a consequence, the LSW predictions underestimate the average cluster radii and density, due to the absence of intermediate asymptotic regime in the LSW theory. At the same time, the ARIMA forecast demonstrates that in the long-time limit the reaction rate, k_1' approaches the LSW results for medium and strong interactions, Table 2, and the LSW theory supersaturation estimates, $k_2 = 7.4{\times}10^{-3}$ and $1.2{\times}10^{-4}$, agree well with the simulation data for medium and strong attractions, respectively, Fig. 4c.

The yttria nano-clusters observed experimentally in ODS alloys have radii of a few nm and clusters density $10^{21} - 10^{23}$ m^{-3}, see Table 2. A typical annealing time of a few hours [5] can be extended to several hundred of hours in the dedicated experiments studying cluster growth kinetics in different temperature limits [9, 11, 12, 37], see Table 2. It was shown that higher temperatures lead to larger average cluster sizes with smaller cluster density with increasing reaction rates.

Our KMC simulations support the general trend in both experiments and earlier KMC simulations [13], that with a decrease of cluster average radii the cluster density increases, see Table 2. In our simulations decrease of cluster radius and increase of cluster density at identical times corresponds to an increase of attraction energies (or decrease of temperature). Alternatively, change of alloy composition by inclusion of different particle sorts (e.g. Ti, Cr, and W) correspondingly affect the average interaction energy and thus corresponds to different KMC simulations with different average interactions.

Simulation results using strong interaction, $\epsilon = -4.23$, (radius 1.5 nm, density $7{\times}10^{23}$ m^{-3}, rate 0.25 nm/h$^{1/3}$, $c_A = 0.005$) with ARIMA forecasting to 90 h at $T = 1100$°C agree quantitatively well with experimental values (radius 2.8 nm, density $5.8{\times}10^{22}$ m^{-3}, rate 0.53 nm/h$^{1/3}$) at $T = 1150$°C. One should note here that experimental temperature is by 50°C higher and annealing time is five times longer, 480 h that correspondingly increase the average cluster radius and decrease cluster density of the KMC simulations.

As a particular example, the experimental data in Table 2 in different temperature limits may be well fitted within our model using attractive interaction $\varepsilon = 0.42$ eV (medium–strong type), Fig. 6. On the basis of these calculations we find, that the dimensionless time required to obtain small clusters, e.g., when $\overline{R(\tau)} = 1$ nm, is independent on temperature and reaches $\tau \sim 10^7$. Similarly, the obtained cluster density $\rho_{cl}(\tau) \sim 5{\times}10^{23}$ m^{-3} have no dependence on temperature, Fig. 6 d-f, (it should be noted, that cluster density decreases with time as $\rho_{cl} \sim \tau^{-1}$). However, the physical time that corresponds to $\tau \sim 10^7$ differs considerably with temperature: 22 s (1400°C), 86 s (1300°C), and 7 min (1200°C). Thus the optimal annealing temperatures to create 1 nm nano-clusters in ODS steels depends on the ability to control the temperature within the material, e.g., the higher annealing temperatures require more accurate temperature control at short times. Annealing the material for longer times would create clusters or larger size and smaller density. It is clear that the onset of cluster formation in real systems is harder to monitor than in KMC simulations due to its statistical nature and thus a temperature/time control could be challenging. These findings agree with experimental data, Table 2, that also demonstrate that smaller cluster radius and higher density is easier to obtain for moderate temperatures, where temperature time control accuracy has smaller effect on

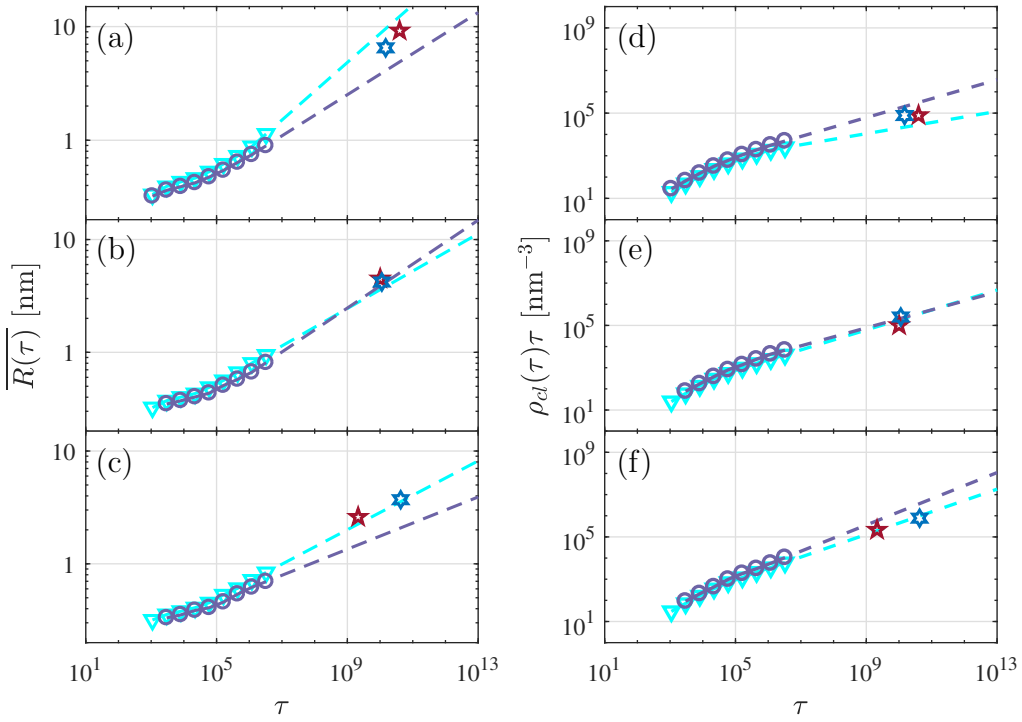

Figure 6: Comparison of KMC simulation kinetics with experimental data in different temperature limits: (a,d) 1400°C, (b,e) 1300°C, and (c,f) 1200°C. For each temperature KMC data obtained from a single calculation for $L = 140a_0$ and $c_A = 0.005$ using $\varepsilon = 0.42$ eV (down triangles) and $\varepsilon = 0.46$ eV (circles) with ARIMA(0,2,0) model forecast (dashed lines). Experimental data pentagram [9] and hexagram [11, 12, 37], Table 2, rescaled to dimensionless time using experimental Y particle jump rate, Table 1.

the cluster kinetics. Different material compositions could alter the average interaction energy, ε, that is used as a fit parameter in our model.

6. Conclusions

We have performed the KMC simulations, to model the yttrium oxide nano-cluster formation and growth in ODS steels. Our simple microscopic oxide formation model has a single particle sort that represents all types of particles involved in cluster formation: yttrium, oxygen atoms, Fe vacancies, that experience an attractive pairwise interaction. Within the model, we have established the solubility–supersolubility phase diagram that (in the particle concentration and attraction energy (temperature) space) separates the unstable zone of a cluster formation from a stable region, where cluster formation is suppressed. Three prototypical particle attraction energies – weak, medium and strong – lead to formation of loose or compact {110}–faceted shape nano-clusters depending on interaction strength.

The methodology is developed for a particle distribution function analysis, that separates the clusters experiencing the OR growth from contribution of small unstable clusters. In particular, it allows us to to follow quantitatively and compare the cluster growth characteristics (average cluster radius, their growth rate, degree of solubility and density) obtained from KMC with both the Lifshitz-Slyozov-Wagner (LSW) theory predictions and ODS experiments. The results for the weak attraction reach the LSW predicted long-time behavior during the typical for ODS steel production time of the order of a few hours. However, these weak interaction results differ strongly from the

experiments suggesting that the average interaction between particles in real materials exceeds weak interaction (0.1 eV) estimate.

In turn, KMC simulations demonstrate that for both medium (0.3 eV) and strong (0.5 eV) attractions the LSW long-time limit is still unreached during a few hours and consequentially results differ from LSW predictions. Instead, the simulations demonstrate new intermediate type kinetics, $\overline{R} \sim t^{1/p}$, that is characterized by different orders p depending on interaction energy. The cluster growth characteristics obtained in simulations with a medium and strong attraction quantitatively well agree with experiments with the p estimates ranging from 5 to 7.6, respectively.

The proposed Y_2O_3 nano-cluster formation model based on homogeneous nucleation is the simplest assumption that mimics particle aggregation in ODS steels. Despite its simplicity, it could provide quantitative estimates and experiment interpretation. The model is complementary to microscopic detailed models but allows us to focus on the cluster formation kinetics in the long-time limit. Moreover, it could be useful for a wide class of systems regarded as many-particle ensembles ranging from numerous physical applications to biological systems [48].

Acknowledgements

This work has been carried out within the framework of the EUROfusion Consortium and has received funding from the Euratom research and training programme 2014-2018 under grant agreement No 633053. The views and opinions expressed herein do not necessarily reflect those of the European Commission.

References

[1] G. Odette, M. Alinger, B. Wirth, Recent developments in irradiation-resistant steels, Annu. Rev. Mater. Res. 38 (2008) 471–503. doi:10.1146/annurev.matsci.38.060407.130315.

[2] G. R. Odette, Recent progress in developing and qualifying nanostructured ferritic alloys for advanced fission and fusion applications, JOM 66 (12) (2014) 2427–2441. doi:10.1007/s11837-014-1207-5.

[3] L. Dai, Y. Liu, Z. Dong, Size and structure evolution of yttria in ODS ferritic alloy powder during mechanical milling and subsequent annealing, Powder Technol. 217 (2012) 281–287. doi:10.1016/j.powtec.2011.10.039.

[4] M. Brocq, B. Radiguet, S. Poissonnet, F. Cuvilly, P. Pareige, F. Legendre, Nanoscale characterization and formation mechanism of nanoclusters in an ODS steel elaborated by reactive-inspired ball-milling and annealing, J. Nucl. Mater. 409 (2) (2011) 80–85. doi:10.1016/j.jnucmat.2010.09.011.

[5] A. London, S. Santra, S. Amirthapandian, B. Panigrahi, R. Sarguna, S. Balaji, R. Vijay, C. Sundar, S. Lozano-Perez, C. Grovenor, Effect of Ti and Cr on dispersion, structure and composition of oxide nano-particles in model ODS alloys, Acta Mater. 97 (2015) 223–233. doi:10.1016/j.actamat.2015.06.032.

[6] S. V. Rogozhkin, N. N. Orlov, A. A. Nikitin, A. A. Aleev, A. G. Zaluzhnyi, M. A. Kozodaev, R. Lindau, A. Möslang, P. Vladimirov, Nanoscale characterization of

13.5% Cr oxide dispersion strengthened steels with various titanium concentrations, Inorg. Mater. Appl. Res. 6 (2) (2015) 151–155. doi:10.1134/S2075113315020136.

[7] C. A. Williams, G. D. Smith, E. A. Marquis, The effect of Ti on the coarsening behavior of oxygen-rich nanoparticles in oxide-dispersion-strengthened steels after annealing at 1200 °C, Scr. Mater. 67 (1) (2012) 108–111. doi:10.1016/j.scriptamat.2012.03.035.

[8] C. A. Williams, P. Unifantowicz, N. Baluc, G. D. Smith, E. A. Marquis, The formation and evolution of oxide particles in oxide-dispersion-strengthened ferritic steels during processing, Acta Mater. 61 (6) (2013) 2219–2235. doi:10.1016/j.actamat.2012.12.042.

[9] J. Shen, H. Yang, Y. Li, S. Kano, Y. Matsukawa, Y. Satoh, H. Abe, Microstructural stability of an as-fabricated 12Cr-ODS steel under elevated-temperature annealing, J. Alloy. Compd. 695 (2017) 1946–1955. doi:10.1016/j.jallcom.2016.11.029.

[10] M. Dadé, J. Malaplate, J. Garnier, F. D. Geuser, N. Lochet, A. Deschamps, Influence of consolidation methods on the recrystallization kinetics of a Fe–14Cr based ODS steel, J. Nucl. Mater. 472 (2016) 143–152. doi:10.1016/j.jnucmat.2016.01.019.

[11] N. Cunningham, M. Alinger, D. Klingensmith, Y. Wu, G. Odette, On nano-oxide coarsening kinetics in the nanostructured ferritic alloy MA957: A mechanism based predictive model, Mater. Sci. Eng. A 655 (2016) 355–362. doi:10.1016/j.msea.2015.12.074.

[12] N. Cunningham, Y. Wu, D. Klingensmith, G. Odette, On the remarkable thermal stability of nanostructured ferritic alloys, Mater. Sci. Eng. A 613 (2014) 296–305. doi:10.1016/j.msea.2014.06.097.

[13] C. Hin, B. D. Wirth, J. B. Neaton, Formation of Y_2O_3 nanoclusters in nanostructured ferritic alloys during isothermal and anisothermal heat treatment: A kinetic Monte Carlo study, Phys. Rev. B 80 (2009) 134118. doi:10.1103/PhysRevB.80.134118.

[14] D. Murali, B. Panigrahi, M. Valsakumar, C. Sundar, Diffusion of Y and Ti/Zr in bcc iron: A first principles study, J. Nucl. Mater. 419 (1–3) (2011) 208–212. doi:10.1016/j.jnucmat.2011.05.018.

[15] L. Barnard, N. Cunningham, G. Odette, I. Szlufarska, D. Morgan, Thermodynamic and kinetic modeling of oxide precipitation in nanostructured ferritic alloys, Acta Mater. 91 (2015) 340–354. doi:10.1016/j.actamat.2015.03.014.

[16] X. Boulnat, M. Perez, D. Fabrgue, S. Cazottes, Y. de Carlan, Characterization and modeling of oxides precipitation in ferritic steels during fast non-isothermal consolidation, Acta Mater. 107 (2016) 390–403. doi:10.1016/j.actamat.2016.01.034.

[17] G. Zvejnieks, V. N. Kuzovkov, Monte Carlo simulations for a Lotka-type model with reactant surface diffusion and interactions, Phys. Rev. E 63 (2001) 051104. doi:10.1103/PhysRevE.63.051104.

[18] E. Tornau, V. Petrauskas, G. Zvejnieks, Surface phase transitions at O and CO catalytic reaction on Pd(111), Catal. Today 116 (1) (2006) 62–68. doi:10.1016/j.cattod.2006.02.081.

[19] G. Zvejnieks, V. Kuzovkov, V. Petrauskas, E. Tornau, Modelling of phase transitions and reaction at CO adsorption on oxygen precovered Pd(111), Appl. Surf. Sci. 252 (15) (2006) 5395–5398. doi:10.1016/j.apsusc.2005.12.048.

[20] G. Zvejnieks, A. Ibenskas, E. Tornau, Effects of pressure, temperature and atomic exchanges on phase separation dynamics in Au/Ni(111) surface alloy: Kinetic Monte Carlo study, J. Alloy. Compd. 649 (2015) 313–319. doi:10.1016/j.jallcom.2015.07.132.

[21] G. Zvejnieks, P. Merzlyakov, V. Kuzovkov, E. Kotomin, Void lattice formation in electron irradiated CaF_2: Statistical analysis of experimental data and cellular automata simulations, Nucl. Instr. Meth. B 368 (2016) 138–143. doi:10.1016/j.nimb.2015.11.037.

[22] G. E. P. Box, G. M. Jenkins, G. C. Reinsel, G. M. Ljung, Time Series Analysis: Forecasting and Control (Fifth Edition), John Wiley and Sons Inc., Hoboken, New Jersey, 2015.

[23] I. Lifshitz, V. Slyozov, The kinetics of precipitation from supersaturated solid solutions, J. Phys. Chem. Solids 19 (1–2) (1961) 35–50. doi:10.1016/0022-3697(61)90054-3.

[24] C. Wagner, Theorie der Alterung von Niederschlägen durch Umlösen (Ostwald-Reifung), Z. Elektrochem. 65 (7–8) (1961) 581–591. doi:10.1002/bbpc.19610650704/full.

[25] J. Schmelzer, D. P. Landau, Monte Carlo simulation of nucleation and growth in the 3D nearest-neighbor Ising model, Int. J. Mod. Phys. C 12 (03) (2001) 345–359. doi:10.1142/S012918310100178X.

[26] G. Barenblatt, Scaling, Self-similarity, and Intermediate Asymptotics: Dimensional Analysis and Intermediate Asymptotics, Cambridge Texts in Applied Mathematics, Cambridge University Press, 1996.

[27] Y. B. Zel'dovich, D. D. Sokolov, Fractals, similarity, intermediate asymptotics, Soviet Physics Uspekhi 28 (7) (1985) 608–616. doi:10.1070/PU1985v028n07ABEH003873.

[28] S. Piskunov, G. Zvejnieks, Y. F. Zhukovskii, S. Bellucci, Atomic and electronic structure of both perfect and nanostructured Ni(111) surfaces: First-principles calculations, Thin Solid Films 519 (11) (2011) 3745–3751. doi:10.1016/j.tsf.2011.01.357.

[29] G. Zvejnieks, A. Ibenskas, E. Tornau, Kinetic Monte Carlo modeling of reaction-induced phase separation in Au/Ni(111) surface alloy, Surf. Coat. Tech. 255 (2014) 15–21. doi:10.1016/j.surfcoat.2013.11.002.

[30] M. Alinger, B. Wirth, H.-J. Lee, G. Odette, Lattice Monte Carlo simulations of nanocluster formation in nanostructured ferritic alloys, J. Nucl. Mater. 367–370, Part A (2007) 153–159. doi:10.1016/j.jnucmat.2007.03.010.

[31] C. Hin, B. Wirth, Formation of oxide nanoclusters in nanostructured ferritic alloys during anisothermal heat treatment: A kinetic Monte Carlo study, Mater. Sci. Eng. A 528 (4–5) (2011) 2056–2061. doi:10.1016/j.msea.2010.11.017.

[32] P. Jegadeesan, D. Murali, B. K. Panigrahi, M. C. Valsakumar, C. S. Sundar, Lattice kinetic Monte Carlo simulation of Y-Ti-O nanocluster formation in bcc Fe, Int. J. Nanosci. 10 (04n05) (2011) 973–977. doi:10.1142/S0219581X11008691.

[33] L. Kittiratanawasin, R. Smith, B. P. Uberuaga, K. E. Sickafus, Radiation damage and evolution of radiation-induced defects in Er_2O_3 bixbyite, J. Phys.: Condens. Matter 21 (11) (2009) 115403. doi:10.1088/0953-8984/21/11/115403.

[34] F. Hanic, M. Hartmanová, G. G. Knab, A. A. Urusovskaya, K. S. Bagdasarov, Real structure of undoped Y_2O_3 single crystals, Acta Cryst. 40 (2) (1984) 76–82. doi:10.1107/S0108768184001774.

[35] W. P. Davey, Precision measurements of the lattice constants of twelve common metals, Phys. Rev. 25 (1925) 753–761. doi:10.1103/PhysRev.25.753.

[36] J.-L. Bocquet, C. Barouh, C.-C. Fu, Migration mechanism for oversized solutes in cubic lattices: The case of yttrium in iron, Phys. Rev. B 95 (2017) 214108. doi:10.1103/PhysRevB.95.214108.

[37] M. Alinger, On the formation and stability of nanometer scale precipitates in ferritic alloys during processing and high temperature service, Ph.D. thesis, University of California, Santa Barbara (September 2004).

[38] V. Kuzovkov, G. Zvejnieks, Reply to "Comment on 'Monte Carlo simulations for a Lotka-type model with reactant surface diffusion and interactions' ", Phys. Rev. E 65 (2002) 033102. doi:10.1103/PhysRevE.65.033102.

[39] J. Mullin, Solutions and solubility, in: J. Mullin (Ed.), Crystallization (Fourth Edition), Butterworth-Heinemann, Oxford, 2001, pp. 86–134. doi:10.1016/B978-075064833-2/50005-X.

[40] A. Baldan, Review Progress in Ostwald ripening theories and their applications to nickel-base superalloys Part I: Ostwald ripening theories, J. Mater. Sci. 37 (11) (2002) 2171–2202. doi:10.1023/A:1015388912729.

[41] M. Strobel, K.-H. Heinig, W. Möller, Three-dimensional domain growth on the size scale of the capillary length: Effective growth exponent and comparative atomistic and mean-field simulations, Phys. Rev. B 64 (2001) 245422. doi:10.1103/PhysRevB.64.245422.

[42] C. D. Lorenz, R. M. Ziff, Precise determination of the bond percolation thresholds and finite-size scaling corrections for the sc, fcc, and bcc lattices, Phys. Rev. E 57 (1998) 230–236. doi:10.1103/PhysRevE.57.230.

[43] P. W. Voorhees, The theory of Ostwald ripening, J. Stat. Phys. 38 (1) (1985) 231–252. doi:10.1007/BF01017860.

[44] G. A. Korn, T. M. Korn, Mathematical Handbook for Scientists and Engineers: Definitions, Theorems, and Formulas for Reference and Review, Dover Publications, Inc., Mineola, New York, 2000.

[45] H. Gleiter, Microstructure, in: R. W. Cahn, P. Haasen (Eds.), Physical Metallurgy (Fourth Edition), North-Holland, Oxford, 1996, pp. 843–942. doi:10.1016/B978-044489875-3/50014-4.

[46] G. Zvejnieks, V. N. Kuzovkov, O. Dumbrajs, A. W. Degeling, W. Suttrop, H. Urano, H. Zohm, Autoregressive moving average model for analyzing edge localized mode time series on Axially Symmetric Divertor Experiment (ASDEX) Upgrade tokamak, Phys. Plasmas 11 (12) (2004) 5658–5667. doi:10.1063/1.1814368.

[47] A. W. Degeling, J. B. Lister, Y. R. Martin, G. Zvejnieks, Were the chaotic ELMs in TCV the result of an ARMA process?, Plasma Phys. Contr. F. 46 (10) (2004) L15–L21. doi:10.1088/0741-3335/46/10/L01.

[48] R. Mahnke, J. Kaupužs, I. Lubashevsky, Physics of Stochastic Processes: How Randomness Acts in Time, Wiley-VCH Verlag GmbH & Co. KGaA, Weinheim, 2009.

			$\overline{R(\tau)}$ [nm]	$\rho_{cl}(\tau)$ [m^{-3}]	k_1' [$nm/h^{1/3}$]	Annealing conditions
KMC simulation results:						
c_A	ϵ	τ				
0.100	−0.85	3×10^6	6	5×10^{22}	9.7	1100°C, 13min
0.100 0.005	−2.54	10^7	2.0	2×10^{24} 2×10^{23}	2.4	1100°C, 40min
0.100 0.005	−4.23	10^7	0.7	4×10^{25} 4×10^{24}	0.9	1100°C, 40min
ARIMA(0,2,0) forecasts:						
0.100 0.005	−2.54	1.3×10^9	7.0	6×10^{22} 5×10^{21}	1.5	1100°C, 90h
0.100 0.005	−4.23	1.3×10^9	1.5	5×10^{24} 7×10^{23}	0.25	1100°C, 90h
LSW results:						
	ϵ	$z_s - z_b$				
	−0.85	−2	5	10^{24}	8	1100°C, 13min
	−2.54	−2	1.1	10^{26}	1.2	1100°C, 40min
	−4.23	−2	0.14	10^{29}	0.15	1100°C, 40min
Experimental results:						
Fe–12Cr–2W–0.3Ti–0.25Y_2O_3 [a]			9.2	2×10^{21}	3.1	1400°C, 24h
Fe–12Cr–2W–0.3Ti–0.25Y_2O_3 [a]			4.5	10^{22}	1.4	1300°C, 24h
Fe–12Cr–2W–0.3Ti–0.25Y_2O_3 [a]			2.6	10^{23}	0.8	1200°C, 24h
Fe–14Cr–0.3Mo–Ti–0.25Y_2O_3 [b]			6.5	5.2×10^{21}	3.4	1400°C, 9h
Fe–14Cr–0.3Mo–Ti–0.25Y_2O_3 [b]			4.2	2.2×10^{22}	1.7	1300°C, 27h
Fe–14Cr–0.3Mo–Ti–0.25Y_2O_3 [b]			3.7	1.8×10^{22}	0.53	1200°C, 480h
Fe–14Cr–0.3Mo–Ti–0.25Y_2O_3 [b]			2.8	5.8×10^{22}	0.53	1150°C, 480h
Fe–14Cr–0.3Mo–Ti–0.25Y_2O_3 [b]			1.5	4.7×10^{23}	0.052	1000°C, 21.9kh

Table 2: KMC simulation result estimates from Fig. 4 at times $\tau = 3\times10^6$ ($t = 13$ min) and $\tau = 10^7$ ($t = 40$ min), respectively, where for conversion we have used experimental Y particle jump rate $\nu = 4\times10^3$ s^{-1} at temperature 1100°C, see Table 1. The LSW theory predictions are obtained from Eq. (16). [a]Data are taken from Ref. [9]. [b]Data for alloy MA957 are from Ref. [11, 12, 37].

Institute of Solid State Physics, University of Latvia as the Center of Excellence has received funding from the European Union's Horizon 2020 Framework Programme H2020-WIDESPREAD-01-2016-2017-TeamingPhase2 under grant agreement No. 739508, project CAMART²